Sensors & Diagnostics

ROYAL SOCIETY OF CHEMISTRY

PAPER

View Article Online
View Journal

Cite this: DOI: 10.1039/d6sd00040a

Cobalt molybdenum oxide nanorod decorated carbon yarn for non-enzymatic electrochemical detection of epinephrine

Pranav Mecheri, Swathi Vaidyanatha Iyer,
Lekshmi Bindu Raveendran and Mini Mol Menamparambath *

Received 16th February 2026,
Accepted 30th April 2026

DOI: 10.1039/d6sd00040a

rsc.li/sensors

Epinephrine (EP), a critical hormone secreted by the adrenal glands, is a vital clinical biomarker linked to various neurological and cardiovascular disorders, making its accurate monitoring essential for diagnosis and patient management. Herein, we report a nonenzymatic electrochemical sensor for EP detection based on carbon yarn (CY) functionalized with cobalt molybdenum oxide (CMO) nanorods. A liquid/liquid interface-assisted strategy using *n*-butanol and water was employed to tailor the growth of CMO nanostructures. Importantly, the influence of metal precursor concentration on morphology evolution and electrochemical performance was systematically investigated. Controlled nanorod architectures of CMO were formed at optimized concentrations, whereas higher concentrations yielded irregular flake-like structures with minor impurity phases and reduced activity. The optimized CMO-modified carbon yarn exhibited excellent electrochemical activity for EP detection, demonstrating high selectivity, stability, repeatability, and a low detection limit of 2.14 nM. The sensor's practical applicability was validated using real samples, including EP injection solutions and human serum. Finally, a flexible device was fabricated, delivering promising performance.

Introduction

Epinephrine is a catecholamine neurotransmitter produced by the adrenal glands and plays a key role in the body's response to stress or fear. During emotional or physical stress, the activation of the sympathoadrenal system stimulates the release of epinephrine, resulting in elevated EP levels in the bloodstream.[1,2] Clinically, EP is also administered to treat conditions such as asthma and severe allergic reactions.[3] Irregular EP concentrations in the body act as a biochemical marker for disorders such as Parkinson's disease, depression, Alzheimer's disease, Schizophrenia, Huntington's disease, and various cardiac conditions.[4–6] Given that these disorders are influenced by altered EP levels, precise and rapid determination of EP in biological fluids is essential for effective clinical diagnosis.

A range of analytical methods is available for the detection of epinephrine, which includes ratiometric,[2] colorimetric,[7] high-pressure liquid chromatography,[8] and surface-enhanced Raman scattering.[9] Although these approaches offer good sensitivity and reliability, many of them require complex instrumentation, extensive sample preparation, and higher operational costs. In contrast, electrochemical sensing has circumvented these barriers and emerged as a more practical and efficient alternative due to its rapid response, simplicity, and low cost. Electrochemical strategies can be broadly classified into enzymatic and non-enzymatic approaches. Enzymatic sensing relies on immobilizing specific enzymes onto the electrode surface, but this process is intricate and requires tightly controlled reaction conditions to maintain enzyme activity. Non-enzymatic electrochemical sensing overcomes these limitations by employing catalytically active electrode materials that directly facilitate the redox reaction of the analyte, enabling stable and reliable detection.[10–12] Metals and metal oxides/hydroxides have therefore become attractive coating materials for non-enzymatic electrochemical sensors owing to their strong catalytic activity, stability, crystallinity, and high surface area.[13–18] When integrated onto the electrode surface, these materials provide abundant active sites, thereby improving sensitivity and overall sensing performance.

In this work, cobalt molybdenum oxide nanostructures were synthesized using a liquid/liquid interface-assisted strategy, employing *n*-butanol and water as two immiscible phases. The influence of metal precursor concentration in the aqueous phase on the material properties was systematically examined. X-ray diffraction (XRD), Raman, and Fourier transform infrared (FTIR) analyses confirmed the successful formation of cobalt molybdenum oxides, while higher

---

Department of Chemistry, National Institute of Technology Calicut, Calicut-673601, Kerala, India. E-mail: minimol@nitc.ac.in

precursor ratios were found to introduce impurity phases. Field-emission scanning electron microscope (FE-SEM) imaging revealed notable morphological changes with varying precursor concentrations. Low and moderate metal concentrations result in nanorod-like morphologies, whereas higher concentrations yield larger flakes. Electrochemical studies using CV and EIS indicated that CY coated with the sample synthesized at 1 mmol of metal precursors in 20 ml of aqueous medium (CM-B) exhibited superior activity. The materials were subsequently coated onto single strands of carbon yarn and assessed for their performance in detecting the neurotransmitter epinephrine. The sensor demonstrated excellent electrocatalytic activity toward EP, with high stability, selectivity, and repeatability. Its real-time applicability was further validated using human serum and EP injection samples. Finally, a flexible, miniaturized version of the sensor was fabricated, showing promising sensing performance.

Materials and methods

All experiments involving human serum samples were performed in accordance with the relevant institutional guidelines and approved by the Institutional Ethics Committee of National Institute of Technology Calicut (Ref. No. EC/21/2025). The study utilized anonymized leftover human serum samples obtained from the Institute Health Center, and therefore, informed consent was waived by the ethics committee.

Chemicals and reagents

Cobalt nitrate hexahydrate (Fisher Scientific, 10026-22-9, 97%), ammonium molybdate tetrahydrate (Fisher Scientific, 12054-85-2, 99%), *n*-butyl alcohol (Fisher Scientific, 71-36-3, 99%), urea (Fisher Scientific, 57-13-6, 99%), ethanol (Sigma Aldrich, 64-17-5, ≥99.8%), potassium ferricyanide (Fisher Scientific, 13746-66-2, 99%), dimethyl sulfoxide (Merck, 67-68-5, > 99%), phosphate buffered saline (pH- 7.4, Himedia, 9004-65-3), epinephrine (Sigma-Aldrich, 51-43-4, 99%) L-ascorbic acid (Thermo Scientific, 50-81-7, 99%), dopamine hydrochloride (Alfa Aesar, 62-31-7, 99%), uric acid (Alfa Aesar, 69-93-2, 99%), L-cysteine (Sigma-Aldrich, 56-89-3, ≥98%), glutamic acid (Sigma-Aldrich, 56-86-0, 99%), sodium chloride (Sigma Aldrich, 7647-14-5, ≥99%), potassium chloride (Fisher Scientific, 7447-40-7, 99.8%), carbon cloth (TES Electrode store, 0.33 mm), polyimide heat resistant adhesive tape (Kapton, 50 mm), transparent polyester films (75 μm thickness, Ganapathi Industries), pyrolytic graphite sheet (Intelligent materials Pvt. Ltd., 7440-44-0), conductive silver paste (Techinstro, Silverpaste-001), copper foil tape (Electomania), deionized water (DI water, ELGA Purelab Quest UV, >18 MΩ).

Synthesis of cobalt molybdenum oxide

Cobalt molybdenum oxides were synthesized *via* a liquid/liquid interface-assisted method using *n*-butanol and water as solvents. Cobalt nitrate hexahydrate and ammonium molybdate tetrahydrate were each dissolved in 10 mL of deionized water, while urea was separately dissolved in 20 mL of *n*-butanol at 90 °C. The aqueous solutions were then slowly introduced along the vessel walls into the hot urea–butanol solution, and the mixture was maintained at 90 °C for 6 h with stirring at 50 rpm. Three parallel syntheses were conducted using equimolar concentrations of cobalt nitrate and ammonium molybdate at 0.5 mmol (CM-A), 1 mmol (CM-B), and 2 mmol (CM-C), as shown in Table S1. The resulting precipitates were washed with an ethanol–water solution (1 : 3, v/v), collected by vacuum filtration, and dried in a hot-air oven at 60 °C to yield the final products.

Material characterization

The crystal structure and crystallinity of the synthesized compounds were analyzed using the X-ray diffraction technique (Rigaku SmartLab SE) operated at 40 kV and 30 mA employing Cu Kα radiation with a wavelength of 1.54 Å. The chemical and structural characteristics of the compounds were examined using Raman spectroscopy (LabRAM HR Evolution Confocal Raman Microscope, 532 nm laser source) and FTIR (JASCO FTIR 4700) analysis. The morphology of the synthesized samples was analyzed using FE-SEM (Hitachi SU 6600) and HR-TEM (TALOS F200S G2, 200 kV), both equipped with EDS and elemental mapping. X-ray photoelectron spectroscopy (XPS, Thermo Fisher, K-Alpha) was employed to investigate the elemental composition and oxidation states of the synthesized material.

Electrode fabrication and electrochemical characterizations

Electrochemical analyses, including cyclic voltammetry (CV), differential pulse voltammetry (DPV), and electrochemical impedance spectroscopy (EIS), were performed using a CHI660E electrochemical workstation. The measurements were conducted in a standard three-electrode configuration, where the material-modified carbon yarn served as the working electrode, Ag/AgCl (aq) acted as the reference electrode, and a platinum wire was used as the counter electrode. To prepare the working electrode, the carbon yarns were carefully detached from the carbon cloth and trimmed into pieces approximately 6 cm in length. These yarns were ultrasonically treated in acetone to remove organic impurities, thoroughly rinsed with distilled water, and dried in an oven at 60 °C. The cleaned yarns were then immersed in a cobalt molybdenum oxide (CMO) dispersion (5 mg mL^{-1}) prepared in DMSO and mechanically agitated for 1 h to ensure uniform deposition of the material onto the carbon surface. Finally, the coated yarns were dried again at 60 °C to remove any residual solvent and enhance material adhesion before being used for electrochemical measurements. 0.1 M phosphate buffer with pH 7.2 was used as the buffer solution throughout the experiments. For the determination of the limit of detection (LOD), DPV measurements were performed using standard epinephrine (EP) solutions prepared in buffer at varying concentrations within a potential range of 100–350 mV. The electrocatalytic behavior and redox kinetics of the electrode material toward EP were further investigated through CV at different scan rates. The selectivity of the developed electrode was evaluated by recording DPV responses in the presence of common interfering species such as uric acid (UA), cysteine (CS), dopamine (DA), glutamic acid (GA), ascorbic acid (AA), NaCl, and KCl, each at a concentration one hundred times higher than that of EP. The sensor's stability was examined by conducting ten consecutive CV cycles, while reproducibility was confirmed by recording CV responses using three independently prepared carbon yarn electrodes. Real sample analysis was conducted in both an epinephrine injection and human serum. The epinephrine injection (R_x adrenaline bitartrate) was obtained from a local pharmacy, and anonymized leftover serum samples were collected from the health center, NITC. A 100 μL aliquot of EP injection and serum was placed in a beaker and diluted tenfold with a buffer solution for electrochemical analysis. Recovery analysis was performed by carrying out DPV by spiking different concentrations of standard epinephrine solution.

For the fabrication of the flexible sensor, a rectangular substrate (5×2 cm^2) was prepared using a transparent polyester film. The surface of the film was laminated with a polyimide heat-resistant adhesive tape to provide mechanical stability and thermal protection. A rectangular strip of pyrolytic graphite sheet was attached to one end of the substrate, serving as the counter electrode. The same pyrolytic graphite surface, coated with silver paste to function as the reference electrode. The material-coated carbon thread was positioned at the center of the substrate to act as the working electrode. Electrical connections for all electrodes were established using copper tape, ensuring stable and low-resistance contact throughout the setup.

Results and discussions

Cobalt molybdenum oxide nanostructures were prepared using a liquid/liquid interface approach, serving as a soft template for controlled growth. In this method, the metal precursor salts were dissolved in the aqueous phase, while urea, acting as a source for the OH^-, was introduced in the *n*-butanol phase. The biphasic mixture was maintained at 90 °C for 6 hours, allowing the reaction to proceed predominantly at the confined interface between *n*-butanol and water. This interfacial region facilitated the nucleation and subsequent growth of the oxide nanostructures. The mechanism of formation can be briefed as follows: urea generates OH^- ions in the organic phase, while in the aqueous medium, ammonium molybdate dissociates to yield heptamolybdate species, which hydrolyse upon interaction with the OH^- ions to form MoO_4^{2-}. These molybdate ions subsequently react with Co^{2+} and water molecules at the interface, resulting in the formation of hydrated cobalt molybdate. The chemical reactions that may lead to the formation of CMO nanostructures are outlined below.[15,19,20]

$$6CO(NH_2)_2 \rightarrow C_3H_6N_6 + 6NH_3 + 3CO_2$$

$$NH_3 + ROH \rightarrow NH_4^+ + OR^-$$

$$OR^- + H_2O \leftrightharpoons ROH + OH^-$$

$$(NH_4)_6Mo_7O_{24}\cdot 4H_2O + H_2O \rightarrow 6NH_4^+ + Mo_7O_{24}^{6-} + 5H_2O$$

$$Mo_7O_{24}^{6-} + 8OH^- \rightarrow 7MoO_4^{2-} + 4H_2O$$

$$7Co^{2+} + 7MoO_4^{2-} + nH_2O \rightarrow 7CoMoO_4\cdot nH_2O$$

The crystal structure and crystallinity of the synthesized compounds were examined using XRD, and the corresponding diffractograms are presented in Fig. 1a. The diffraction patterns confirm the formation of monoclinic cobalt molybdenum oxide hydrate ($CoMoO_4\cdot nH_2O$) in all samples, consistent with the ICDD reference pattern 00-026-0477. A schematic representation of the crystal structure generated using VESTA is illustrated in Fig. 1b. Notably, the CM-C sample, prepared at a higher precursor concentration, exhibits additional diffraction peaks corresponding to cobalt hydroxide (ICDD 00-046-0605) and residual ammonium molybdate (ICDD 00-027-1013), indicating the presence of minor impurities. The formation of these secondary phases can be attributed to incomplete interfacial reaction kinetics under high precursor concentration, where excess cobalt ions tend to hydrolyze, leading to the precipitation of $Co(OH)_2$, while the surplus molybdate ions reprecipitate as ammonium molybdate. In contrast, CM-A and CM-B exhibit relatively pure-phase cobalt molybdenum oxide without secondary phases. Among all the samples, CM-B displays the highest peak intensity and sharpest diffraction features, indicative of superior crystallinity of a well-ordered crystal structure.

The vibrational characteristics of the synthesized compounds were further investigated using Raman spectroscopy, and the corresponding spectra are shown in Fig. 1c. The intense bands observed at approximately 929 cm^{-1} and 868 cm^{-1} are assigned to the Co–O–Mo stretching vibrations of CMO.[21,22] The band at 810 cm^{-1} corresponds to the asymmetric stretching of O–Mo–O, while the bands at 334 and 361 cm^{-1} are attributed to the asymmetric and symmetric bending modes of O–Mo–O, respectively.[21,23] In the CM-C sample, additional peaks indicating the presence of impurity phases appeared at 219, 723, and 944 cm^{-1} for ammonium molybdate[24] and 460 cm^{-1} for cobalt hydroxide,[15,25] in agreement with the XRD observations. FTIR analysis was conducted in the range of 400–4000 cm^{-1}, and the

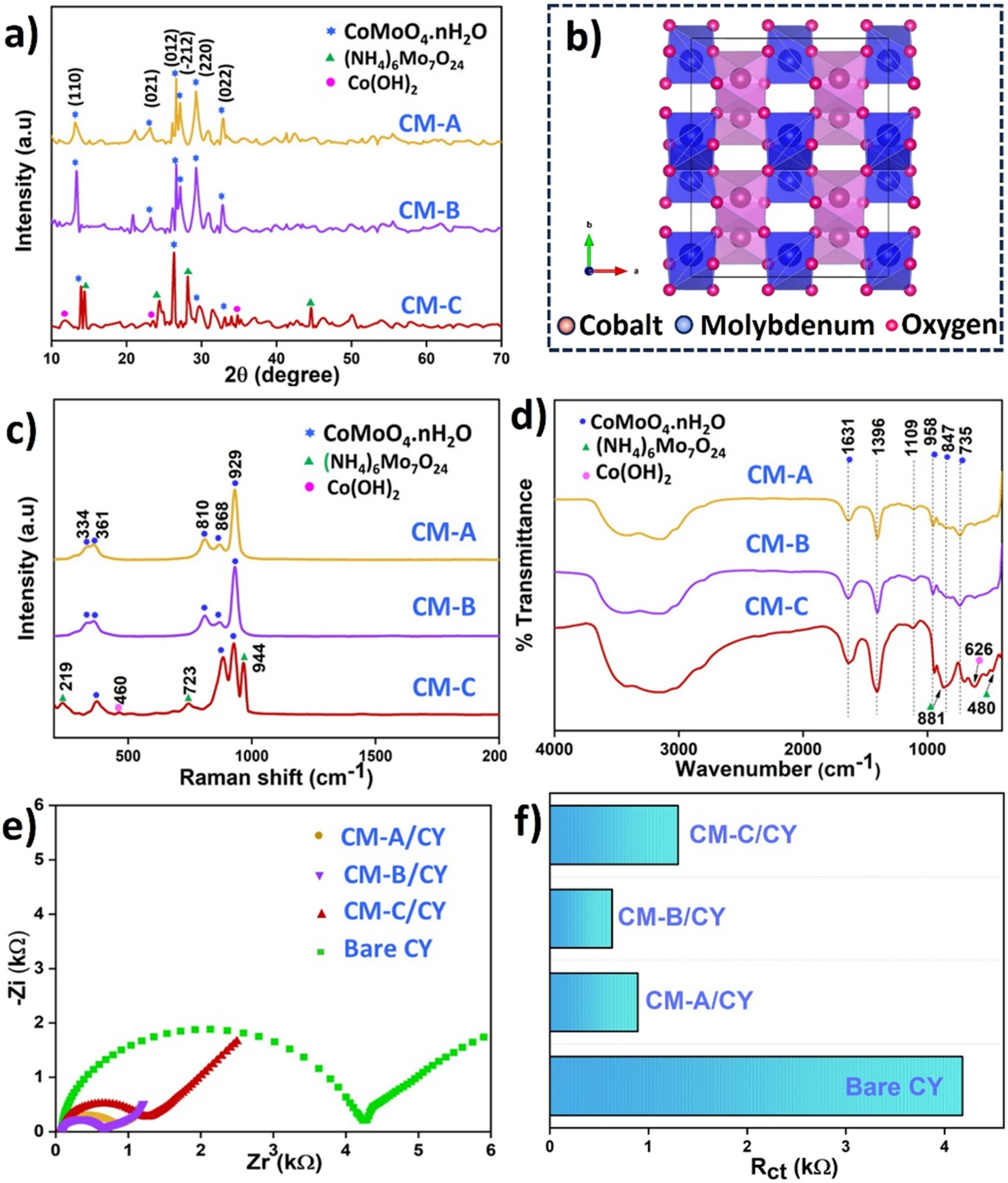

Fig. 1 (a) XRD patterns, (b) schematic view of the crystal structure, (c) Raman spectra, (d) FTIR spectra, (e) EIS spectra, and (f) bar graph showing R_{ct} values of bare and CMO-coated carbon yarns.

corresponding spectrum is shown in Fig. 1d. The bands around 735, 847, and 958 cm^{-1} correspond to the stretching and bending vibrations of Mo–O–Mo in the MoO_4^{2-} unit.[26] A broad band around 3000–3500 and 1631 cm^{-1} is assigned to bending and stretching vibrations of crystallisation or adsorbed water.[26] Bands that are observed at 1396 and 1109 cm^{-1} are likely to be associated with the intercalation of NO_3^{2-}, CO_3^{2-} ions, respectively.[27,28] Similar to the XRD and Raman results, the CM-C sample exhibits additional impurity-related bands. The signals observed at 881 and 480 cm^{-1} are assigned to the Mo═O stretching and Mo–O–Mo flexural modes of ammonium molybdate,[29] while the band at 626 cm^{-1} corresponds to the δ(Co–O–H) vibration of cobalt hydroxide.[30]

The charge transfer characteristics of the synthesized compounds were evaluated using EIS with CMO-coated carbon yarn as working electrodes. The corresponding Nyquist plots for the coated and bare electrodes are shown in Fig. 1e. Each plot displays a semicircular region followed by a linear portion, where the diameter of the semicircle corresponds to the charge transfer resistance (R_{ct}). The equivalent electrical circuits used for fitting are presented in Fig. S1. The electrodes coated with the synthesized samples exhibit significantly lower R_{ct} values compared to the bare electrode (Fig. 1f), confirming their enhanced charge transfer characteristics. Among the tested samples, CM-B/CY demonstrates the lowest R_{ct}, indicating superior charge transfer capability, facilitating the electrochemical activity of the electrodes.

The morphology of the synthesized nanostructures was examined using SEM, as shown in Fig. 2a–c & S2a–c. Samples CM-A and CM-B exhibit nanorod-like morphologies, whereas CM-C displays a agglomerated flake-like structure. In solution-phase nanocrystal growth, both surface reaction and mass transport through the boundary layer can act as the rate-determining step, depending on precursor concentration and localised diffusion characteristics.[31,32] In the present system, increasing the metal ion concentration enhances nucleation density and reduces diffusion length, thereby promoting faster ion supply to the growing crystal. Consequently, the growth rate is limited by the surface reaction, resulting in surface-controlled growth and the formation of flake-like morphologies. In contrast, at lower precursor concentrations, the slower ion diffusion renders mass transport the rate-limiting step, resulting in anisotropic, diffusion-controlled growth of nanorods. The average diameter of CM-A nanorods is about 600 nm, that of CM-B ranges from 300 to 500 nm, and the flake thickness in CM-C is approximately 270 nm.

The morphology and crystallinity of CM-B were further evaluated by TEM and SAED, as shown in Fig. 2d–g. TEM images Fig. 2d and e reveal uniformly distributed, rod-like nanostructures of 223 nm thickness with smooth surfaces and well-defined morphology. The high-resolution TEM image (Fig. 2f) clearly displays distinct and periodic lattice fringes with an interplanar spacing of 3.3 Å, corresponding to the (012) plane, consistent with the XRD results. The continuous and uninterrupted lattice fringes across the entire nanorod indicate a coherent crystal lattice without defects or misorientations, confirming its single-crystalline nature. The SAED pattern (Fig. 2g) reveals sharply defined Bragg spots indexed to distinct crystal planes, further corroborating the

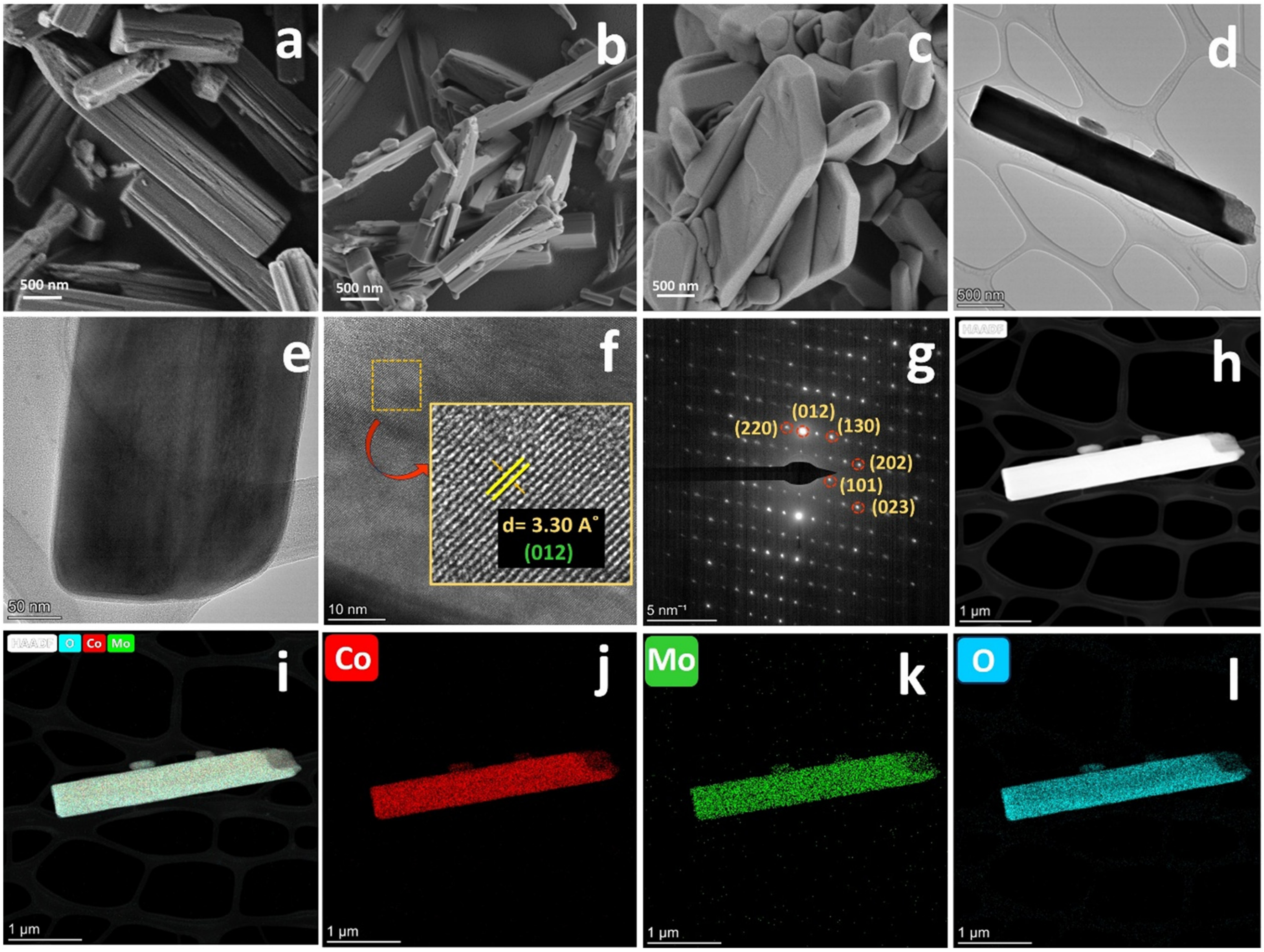

Fig. 2 SEM images of CM-A (a), CM-B (b), and CM-C (c); HR-TEM images of CM-B at two different magnifications (d and e), HR-TEM images with *d* spacing (f), SAED pattern (g); HAADF (h) STEM (i) image of CMO and elemental mapping images of cobalt (j), molybdenum (k), and oxygen (l).

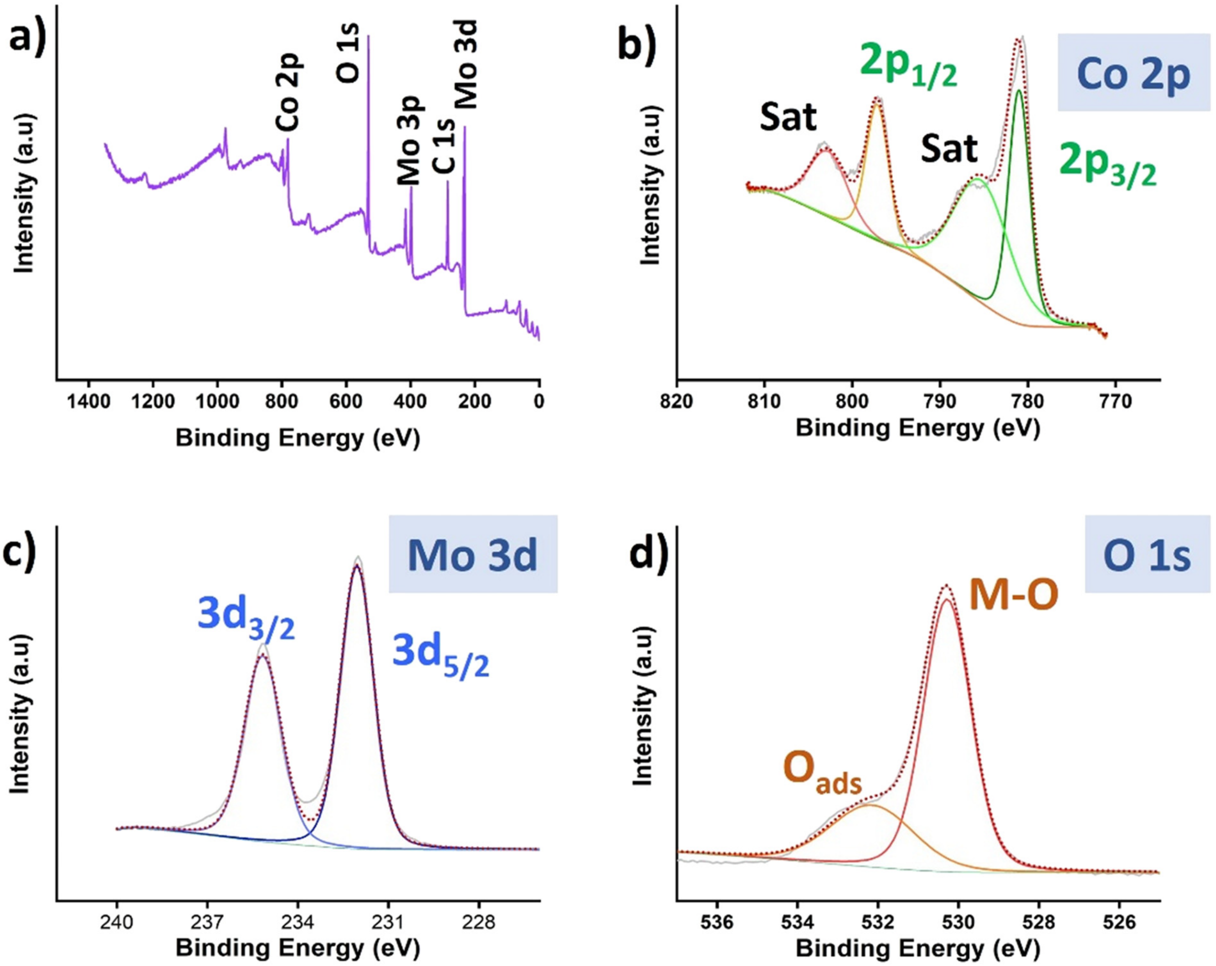

Fig. 3 XPS spectra of CM-B: survey scan (a), deconvoluted spectra of cobalt (b), molybdenum (c), and oxygen (d).

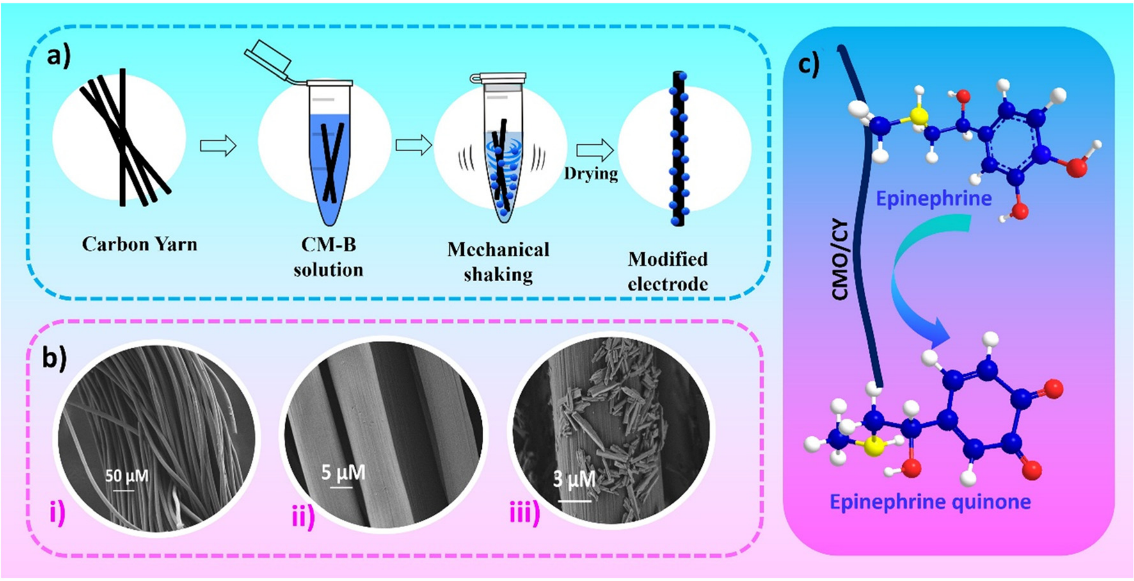

Fig. 4 (a) Schematics of preparation of CMO-coated carbon yarn. (b) SEM images of carbon yarns (i and ii – bare carbon yarn at different resolutions, iii- CMO-coated carbon yarn). (c) Schematics of the electrochemical oxidation of epinephrine to epinephrine quinone at the surface of carbon yarn coated with CMO.

single-crystalline nature and high degree of structural order in CM-B nanorods. Together, these results demonstrate that the synthesized CM-B nanorods possess superior crystallinity and atomic uniformity. The distribution of elements in the crystal was subsequently analyzed by TEM mapping, and the corresponding mapping images are given in Fig. 2h–l. The EDS spectrum shown in Fig. S3 further supports these results. The uniform distribution of cobalt, molybdenum, and oxygen confirms the homogeneous composition and successful formation of CMO.

The chemical states of the elements in the CMO sample were analyzed using XPS, and the corresponding survey and deconvoluted spectra are presented in Fig. 3. The survey spectrum (Fig. 3a) confirms the presence of cobalt, molybdenum, and oxygen in the material. The high-resolution Co 2p spectrum (Fig. 3b) displays distinct peaks at 781.1 eV and 797.1 eV, assigned to Co $2p_{3/2}$ and Co $2p_{1/2}$, respectively, along with two shake-up satellite peaks at 785.7 eV and 802.9 eV, indicating the presence of Co^{2+} species.[33,34] The deconvoluted Mo 3d spectrum, as depicted in Fig. 3c, shows peaks at 232.0 eV and 235.2 eV, corresponding to Mo $3d_{5/2}$ and Mo $3d_{3/2}$, respectively, confirming the presence of Mo in the +6 oxidation state.[34,35] The O 1s spectrum (Fig. 3d) exhibits peaks at 530.3 eV and 532.2 eV, where the lower binding energy peak is attributed to lattice oxygen (metal–oxygen bonds), while the higher energy peak is related to surface-adsorbed oxygen species.[35,36]

The synthesized materials were subsequently coated onto carbon yarns peeled off from carbon cloth for electrochemical characterization. A detailed schematic representation of the process is provided in Fig. 4a. Carbon

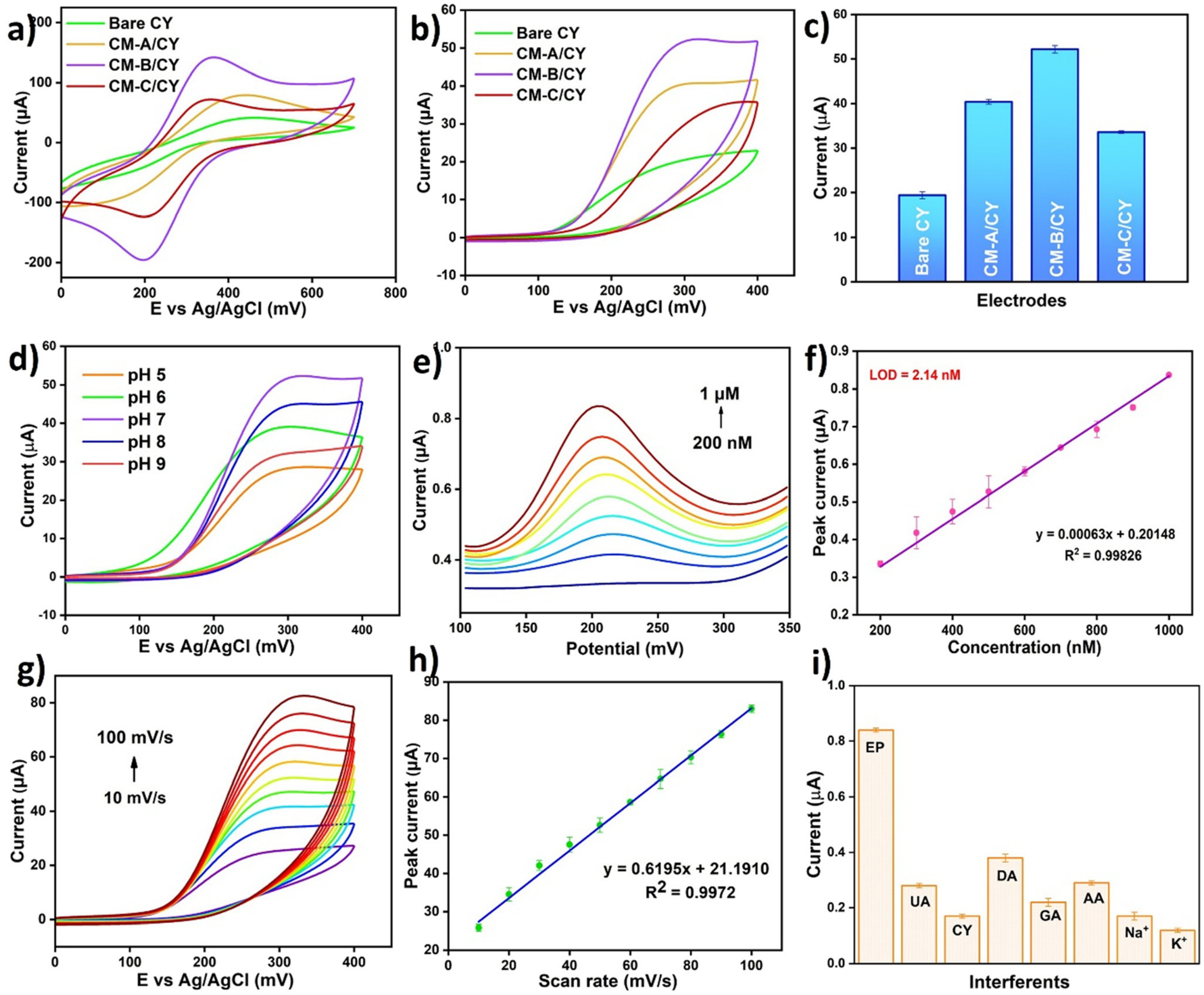

Fig. 5 Cyclic voltammogram of bare and CMO-coated carbon yarns (a) in 5 mM $K_3[Fe(CN)_6]$ in 0.1 M KCl, (b) in 1 millimolar EP in 0.1 M PBS. (c) Bar graph showing current responses of working electrodes in 1 millimolar EP in 0.1 M PBS. (d) CV of CM-B/CY at different pH. (e) DPV of CM-B/CY at different concentrations from 200 nM to 1 μM, (f) corresponding calibration plot of peak current *vs.* concentration of EP. (g) CV of CM-B/CY in 1 millimolar of EP at different scan rates, (h) corresponding calibration plot of peak current *vs.* scan rate. (i) Current responses of 1 μM EP and 100 μM of different interfering agents at 0.1–0.35 V.

yarns, each approximately 6 cm in length, were first pretreated with acetone to remove any surface impurities or organic residues adsorbed. The pretreated yarns were then dried in an oven maintained at 60 °C to ensure complete removal of residual solvent. Following the cleaning step, the yarns were immersed in a well-dispersed CMO suspension prepared in DMSO and mechanically agitated for one hour to promote uniform deposition of the active material onto the carbon fibers. Finally, the coated yarns were dried in an oven to obtain the CMO-coated carbon yarn electrodes with a stable and adherent surface layer. The SEM images of the bare carbon yarn (i, ii) and CMO-coated yarns (iii) are given in Fig. 4b. This CMO-coated carbon yarn was used as the working electrode for all electrochemical measurements. The schematic representation of the oxidation of epinephrine at the surface of CMO-coated carbon yarn (CMO/CY) is given in Fig. 4c.

The electrochemical activity of the prepared materials was evaluated using cyclic voltammetry in 5 mM $K_3[Fe(CN)_6]$ containing 0.1 M KCl, and the corresponding voltammogram is shown in Fig. 5a. As evident from the figure, the CM-B/CY sample exhibits significantly higher redox peak currents than bare carbon yarn as well as CM-A/CY and CM-C/CY coated yarns, indicating its superior electrochemical activity. To further assess the materials' performance toward epinephrine sensing, CV was performed in 1 mM EP prepared in PBS (Fig. 5b). It further validates that CM-B/CY delivers the highest peak current response among all samples, as shown in Fig. 5c. This enhanced electrochemical performance of CM-B/CY is attributed to its relatively smaller sized nonorods with an expected higher surface area compared to CM-A. Furthermore, the CM-C shows highly agglomerated nonoflake-like structures, which may reduce the accessibility of the active surface area for electrochemical reactions. The presence of impurity phases will also disrupt the continuity of the electroactive matrix in CM-C, which introduces interfacial heterogeneity, leading to inefficient electron-ion transport and diminished overall electrochemical performance. The optimum pH for EP electrocatalytic detection was determined by performing CV and DPV

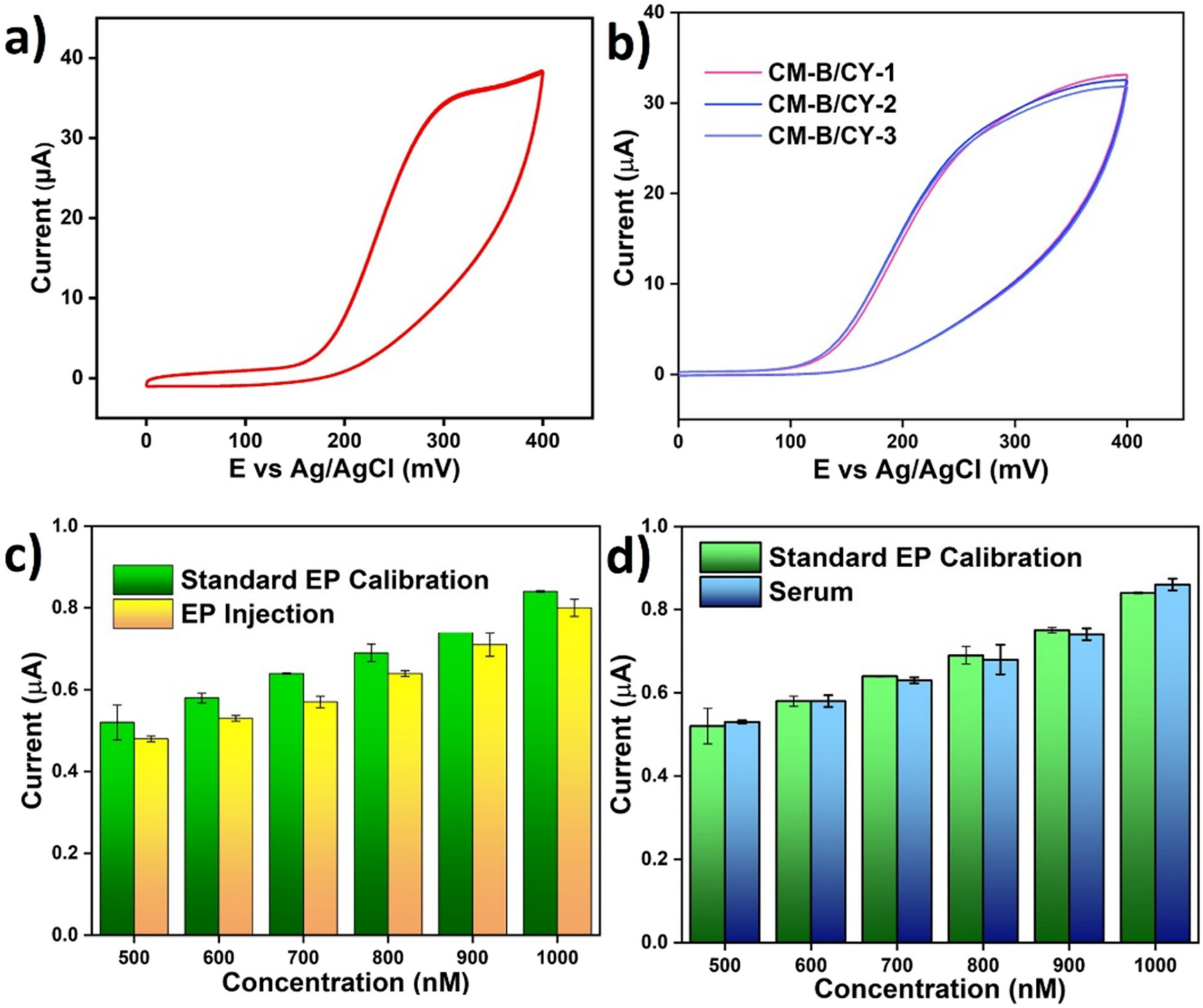

Fig. 6 (a) Cyclic voltammogram of CM-B/CY in 0.5 millimolar of EP in 20 cycles. (b) CV of three different carbon yarns coated with CM-B in 400 μM EP at 50 mV s^{-1} scan rate. (c) Recovery plot of EP detection in EP injection, (d) recovery plot of EP detection in human serum.

measurements at pH values ranging from 5 to 9, and the corresponding graphs are presented in Fig. 5d and S4, respectively. Based on the highest anodic current response, pH 7 was identified as the optimal condition for electrocatalytic oxidation of EP. DPV analysis was performed at varying EP concentrations to determine the lowest limit of detection (Fig. 5e). The corresponding calibration curve, showing the relationship between peak current and concentration, is plotted in Fig. 5f. The curve follows the linear regression equation $y = 0.0006x + 0.2015$ with an R^2 value of 0.9982. The limit of detection (LOD) was calculated using the standard equation LOD = $3S_b/m$, where S_b is the standard deviation of the blank signal and m is the slope of the calibration plot. The resulting LOD was 2.14 nM, which is comparable to or even better than previously reported values, as illustrated in Table S2.

The electrocatalytic mechanism at the electrode surface was evaluated by the scan rate. For this, CV was performed at different scan rates ranging from 10 to 100 mV s^{-1}, as shown in Fig. 5g. The calibration plot of peak current *versus* scan rate is given in Fig. 5h. This plot follows the linear regression equation $y = 0.6195x + 21.1910$ with an R^2 value of 0.9972. The linear nature of this curve indicates that the electrocatalytic mechanism at the electrode surface is surface-controlled. The influence of common interfering species on EP detection was assessed by performing DPV measurements (Fig. S5) using 1 μM EP in the presence of interfering agents at 100-fold higher concentrations (100 μM). The corresponding current responses in the preferred potential range are presented in Fig. 5i as a bar graph. The markedly lower currents obtained for the interfering species compared to EP confirm the high selectivity of the prepared material toward EP detection.

Stability and repeatability are other important factors that influence the application of sensors. The stability of the sensor was evaluated by conducting 10 continuous cycles of CV in 0.5 mM EP at a scan rate of 50 mV s^{-1}, and the corresponding curve is shown in Fig. 6a. A perfect overlap of each cycle with 99.32% retention of anodic current (0.24% RSD) indicates the sensor's high stability. Repeatability of the sensor was tested by carrying out CV using three different carbon yarns coated with CMO (Fig. 6b). The anodic current obtained for each electrode was almost similar, demonstrating the sensor's remarkable reproducibility. Since EP serves as an important neurotransmitter and regulates several vital physiological functions, accurately detecting its levels in real biological and medicinal samples is essential. Therefore, the applicability of the sensor was evaluated using real samples, including EP injection and human serum. Both solutions were diluted 20 times with 0.1 M PBS prior to electrochemical detection. Standard EP solutions were prepared, and known concentrations of these solutions were spiked into the diluted real samples. The DPV curves and the corresponding parameters for recovery of different additions are given in Fig. S6 and Table S3 for EP injection, and Fig. S7 and Table S4 for serum. The comparative current responses for the EP injection and serum with the standard EP solution are illustrated in Fig. 6c and d, respectively. The comparable current for both the real

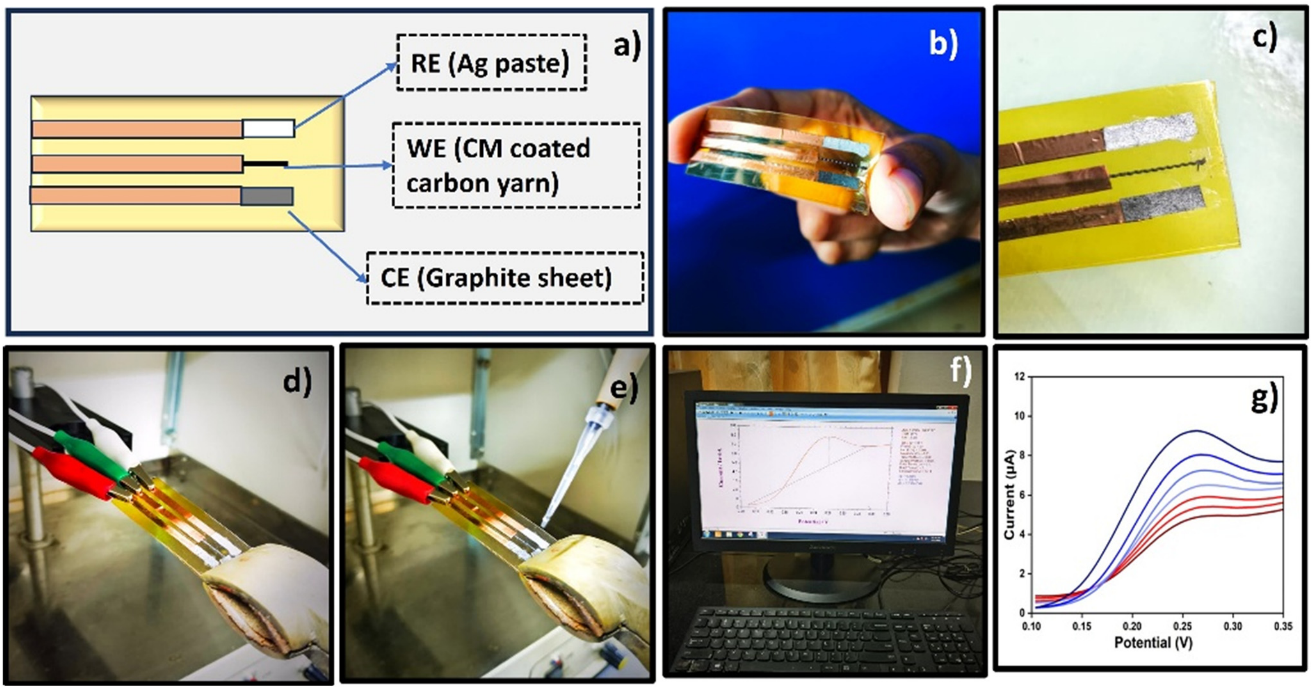

Fig. 7 (a) Schematic representation of flexible electrode, (b and c) photographic image of flexible electrode, (d–f) photographic image of electrochemical analysis using flexible electrode, (g) DPV result of flexible electrode at different EP concentration (100–200 μM).

sample and the standard solution indicates the efficacy of the proposed sensor in detecting real samples.

A flexible, miniaturized form of the sensor was fabricated to check the practical usage of the sensor. Here, a polyimide-taped polyester film was employed as the substrate. The counter electrode was made from a pyrolytic graphite sheet, and the reference electrode was formed by applying a layer of conductive silver paste onto the graphite sheet. The CMO-coated carbon yarn positioned at the center functioned as the working electrode. The structural schematic and photographic images of the fabricated sensor are shown in Fig. 7a and b–f, respectively. DPV analysis was done using the sensor at different EP concentrations (100–200 μM), and the response obtained for the EP solutions is given in Fig. 7g. With increasing EP concentration, the peak current exhibited a gradual rise, confirming the sensor's potential applicability for practical EP detection.

Conclusion

In this work, we successfully developed a cobalt molybdenum oxide-modified electrochemical sensing platform for the rapid and cost-effective detection of epinephrine. The CMO nanostructures were synthesized *via* a liquid/liquid interface-assisted strategy and exhibited a concentration-dependent morphological evolution from nanorods at lower and moderate concentrations to irregular flakes at higher concentrations. Among the fabricated electrodes, CM-B/CY demonstrated superior electrocatalytic activity toward epinephrine detection, achieving a low detection limit of 2.14 nM along a wide linear range of 200–1000 nM. The sensor exhibits excellent selectivity against common interferents, long-term stability, and high repeatability. Successful validation in epinephrine injection samples and human serum confirmed the practical reliability of the sensor under real-world conditions. A flexible, miniaturized prototype further confirms its viability for point-of-care applications, collectively establishing CMO- modified carbon yarn electrodes as promising candidates for next-generation electrochemical biosensors in clinical and healthcare applications.

Author contributions

The manuscript was written with the contribution of all authors. The final version of the manuscript has been approved by all authors.

Conflicts of interest

The authors declare no conflict of interest.

Data availability

The data supporting this article have been included as part of the supplementary information (SI).

Supplementary information: experimental details of the interface-assisted synthesis of CMO with their corresponding product code. EIS equivalent circuits of bare carbon yarn, CMO-coated carbon yarns. EDS spectra of CM-B. Comparison of electrochemical sensors for EP detection. DPV of EP and interfering agents. DPV of serum at different additions of standard EP. Recovery results of EP in EP injection. DPV of serum at different additions of standard EP. Recovery results of EP in serum. See DOI: https://doi.org/10.1039/d6sd00040a.

Acknowledgements

The authors greatly acknowledge the Department of Physics, NIT Calicut, for the XRD measurements; CMC-NIT Calicut, for the Raman analysis; and DST-FIST, for the FE-SEM facility. The authors thank C. R. F. CeNS, Bengaluru, for the HR-TEM facility and JNCASR, Jakkur, Bangalore, for the XPS facility. The authors acknowledge Ms. Aiswarya Chandran for valuable discussions on making a crystal structure using the VESTA software, and Ayisha Liba and Amna Assis K. for their contributions to experimental optimization. The authors also thank Mrs. Haneena KP and the Institute Health Center of the National Institute of Technology Calicut for their assistance with real-world application studies using human serum.

References

1 M. Punniyamoorthy, C. Soosaimanickam, M. Kathiresan and S. Alwarappan, 2D Nb2C MXene/COF Composite as Electrochemical Platform for the Stress Marker Epinephrine Detection, *ACS Appl. Nano Mater.*, 2025, **8**, 19771–19778.

2 U. Mohapatro, P. K. Senapati, S. K. Bhutia and S. Mohapatra, Carbon Dot Fluorescent Nanoprobe for Dual-Channel Detection of Epinephrine and Pyrophosphate in Live Cells, *Anal. Chem.*, 2025, **97**(51), 28310–28322.

3 X. Yang, P. Zhao, Z. Xie, M. Ni, C. Wang, P. Yang, Y. Xie and J. Fei, Selective Determination of Epinephrine Using Electrochemical Sensor Based on Ordered Mesoporous Carbon/Nickel Oxide Nanocomposite, *Talanta*, 2021, **233**, 122545.

4 A. O. Viviano-posadas, J. Valdes-garcía, M. K. Salomón-flores, D. Martínez-otero, J. M. Bautista-renedo, N. González-rivas, H. Sánchez-vidal, J. M. German-acacio, J. Valdés-martínez and A. Dorazco-gonzález, Fluorescent Chemosensing of Epinephrine by a Bis-Boronic Molecular Receptor in Aqueous Media: Crystal Structure, Spectroscopic Studies and Visual Detection, *Dalton Trans.*, 2025, **54**, 12259–12276.

5 M. Jiang, D. Zeng, X. Zheng and H. Yuan, Detection of Epinephrine Using a K2Fe4O7 Modified Glassy Carbon Electrode, *RSC Adv.*, 2024, **14**, 15408–15412.

6 P. Shaikshavali, T. M. Reddy, T. V. Gopal, G. Venkataprasad, V. S. Kotakadi, V. N. Palakollu and R. Karpoormath, A Simple Sonochemical Assisted Synthesis of Nanocomposite (ZnO/MWCNTs) for Electrochemical Sensing of Epinephrine in Human Serum and Pharmaceutical Formulation, *Colloids Surf., A*, 2020, **584**, 124038.

7 S. U. Rehman, S. M. Babulal and H. Wu, Oxygen-Deficient Mn 2 O 3 Nanosheets for Dual Colorimetric and Electrochemical Detection of Epinephrine, *ACS Appl. Nano Mater.*, 2024, **7**, 25004–25013.

8 L. Ma, T. Zhao, P. Zhang, M. Liu, H. Shi and W. Kang, Determination of Monoamine Neurotransmitters and Metabolites by High- Performance Liquid Chromatography Based on Ag(III) Complex Chemiluminescence Detection, *Anal. Biochem.*, 2020, **593**, 113594.

9 A. Dowek, F. Voisin, L. Le, J. M. Mallet and E. Caudron, Self-Assembly of Gold Nanoparticles by Chitosan for Improved Epinephrine Detection Using a Portable Surface Enhanced Raman Scattering Device, *Talanta*, 2023, **251**, 1–10.

10 A. Shadlaghani, M. Farzaneh, D. Kinser and R. C. Reid, Direct Electrochemical Detection of Glutamate, Acetylcholine, Choline, and Adenosine Using Non-Enzymatic Electrodes, *Sensors*, 2019, **19**(3), 447.

11 W. C. Lee, K. B. Kim, N. G. Gurudatt, K. K. Hussain, C. S. Choi, D. S. Park and Y. B. Shim, Comparison of Enzymatic and Non-Enzymatic Glucose Sensors Based on Hierarchical Au-Ni Alloy with Conductive Polymer, *Biosens. Bioelectron.*, 2019, **130**, 48–54.

12 A. Sugunan, A. V. Rethnakumaran and M. M. Menamparambath, A Review on Ti3C2Tx Based Nanocomposites for the Electrochemical Sensing of Clinically Relevant Biomarkers, *Sens. Diagn.*, 2024, **3**, 1769–1788.

13 X. Yu, Z. Liu and X. Huang, Nanostructured Metal Oxides/Hydroxides-Based Electrochemical Sensor for Monitoring Environmental Micropollutants, *Trends Environ. Anal. Chem.*, 2014, **3**, 28–35.

14 P. Kannan and G. Maduraiveeran, Metal Oxides Nanomaterials and Nanocomposite-Based Electrochemical Sensors for Healthcare Applications, *Biosensors*, 2023, **13**(542), 1–18.

15 P. Mecheri, P. Hareesh and M. M. Menamparambath, Tailoring the Morphology of α-Cobalt Hydroxide Using Liquid/Liquid Interface and Its Application in Electrochemical Detection of Ascorbic Acid, *Langmuir*, 2025, **41**, 9422–9433.

16 R. R. Poolakkandy, N. A. Ramalakshmi, K. A. Padmalayam, R. G. Krishnamurthy and M. M. Menamparambath, Braided Copper Cobaltite/MWCNT Composites Enable Acetylcholine Detection at Sub-Nanomolar Levels in Vitro†, *Sens. Diagn.*, 2023, **2**(3), 726–735.

17 A. G. Bindu and R. S. Bhat, Chromium Titanium Yttrium Oxide Nanocomposites Used to Modify Carbon Paste Electrode for Simultaneous Voltammetric Study of 4-Aminophenol and 4-Acetamidophenol, *Adv. Eng. Mater.*, 2026, 1–15.

18 A. G. Bindu and R. S. Bhat, Electrochemical Detection of Rutin in Tomato Sample Using Titanium Dioxide Nanoparticle-Modified Carbon Paste Electrode, *J. Food Meas. Charact.*, 2026, 1–14.

19 C. Wang, E. Zhou, W. He, X. Deng, J. Huang, M. Ding, X. Wei, X. Liu and X. Xu, Nico2o4-Based Supercapacitor Nanomaterials, *Nanomaterials*, 2017, **7**(2), 1–24.

20 W. Wang, Y. Hu, J. Goebl, Z. Lu, L. Zhen and Y. Yin, Shape- and Size-Controlled Synthesis of Calcium Molybdate Doughnut-Shaped Microstructures, *J. Phys. Chem. C*, 2009, **113**(37), 16414–16423.

21 L. Q. Mai, F. Yang, Y. L. Zhao, X. Xu, L. Xu and Y. Z. Luo, Hierarchical MnMoO4/CoMoO4 Heterostructured Nanowires with Enhanced Supercapacitor Performance, *Nat. Commun.*, 2011, **2**(1), 381.

22 G. Harichandran, S. Radha, J. Yesuraj and B. Muthuraaman, Synthesis and Characterization of Cobalt Molybdate Dihydrate Nanorods Arrays for Supercapacitor Electrode Application, *Appl. Phys. A: Mater. Sci. Process.*, 2021, **127**(8), 1–8.

23 A. P. De Moura, L. H. De Oliveira, P. F. S. Pereira, I. L. V. Rosa and M. S. Li, Photoluminescent Properties of CoMoO4 Nanorods Quickly Synthesized and Annealed in a Domestic Microwave Oven, *Adv. Chem. Eng. Sci.*, 2012, **2**, 465–473.

24 C. Li, UV Resonance Raman Spectroscopic Studies on the Genesis of Highly Dispersed Surface Molybdate Species on γ-Alumina, *J. Phys. Chem. B*, 2000, **104**(15), 3581–3588.

25 J. Yang, H. Liu, W. N. Martens and R. L. Frost, Synthesis and Characterization of Cobalt Hydroxide, Cobalt Oxyhydroxide, and Cobalt Oxide Nanodiscs, *J. Phys. Chem. C*, 2010, **114**, 111–119.

26 K. Wang, Y. Li, J. Hu, Z. Lu, J. Xie, A. Hao and Y. Cao, Deep Reconstruction of Transition Metal Molybdate@hydroxide Heterostructure Triggered by Anion-Exchange Reaction as High Efficiency Water Oxidation Electrocatalyst, *Chem. Eng. J.*, 2022, **447**, 137540.

27 Z. Liu, R. Ma, M. Osada, K. Takada and T. Sasaki, Selective and Controlled Synthesis of α- and β-Cobalt Hydroxides in Highly Developed Hexagonal Platelets, *J. Am. Chem. Soc.*, 2005, **127**(40), 13869–13874.

28 M. Dixit, G. N. Subbanna and P. V. Kamath, Homogeneous Precipitation from Solution by Urea Hydrolysis: A Novel Chemical Route to the α-Hydroxides of Nickel and Cobalt, *J. Mater. Chem.*, 1996, **6**(8), 1429–1432.

29 L. Yang, X. Li, T. Qi, G. Liu, Z. Peng and Q. Zhou, Direct Synthesis of Pure Ammonium Molybdates from Ammonium Tetramolybdate and Ammonium Bicarbonate, *ACS Sustainable Chem. Eng.*, 2020, **8**(49), 18237–18244.

30 Z. Huang, Y. Zhao, Y. Song, Y. Li, G. Wu, H. Tang and J. Zhao, Study on the Oxidation Process of Cobalt Hydroxide to Cobalt Oxides at Low Temperatures, *RSC Adv.*, 2016, **6**(83), 80059–80064.

31 J. M. Lee, Y. S. No, S. Kim, H. G. Park and W. I. Park, Strong Interactive Growth Behaviours in Solution-Phase Synthesis of Three-Dimensional Metal Oxide Nanostructures, *Nat. Commun.*, 2015, **6**, 1–7.

32 H. Sharifi Dehsari, A. Halda Ribeiro, B. Ersöz, W. Tremel, G. Jakob and K. Asadi, Effect of Precursor Concentration on Size Evolution of Iron Oxide Nanoparticles, *CrystEngComm*, 2017, **19**(44), 6694–6702.

33 M. Zang, N. Xu, G. Cao, Z. Chen, J. Cui, L. Gan, H. Dai, X. Yang and P. Wang, Cobalt Molybdenum Oxide Derived High-Performance Electrocatalyst for the Hydrogen Evolution Reaction, *ACS Catal.*, 2018, **8**(6), 5062–5069.

34 H. Tong, S. Xu, X. Zheng, M. Qi, J. Zhu, D. Li and D. Jiang, Constructing Dense CoRu-CoMoO4 Heterointerfaces with

Electron Redistribution for Synergistically Boosted Alkaline Electrocatalytic Water Splitting, *Small*, 2025, **21**(3), 1–11.

35 F. Nti, D. A. Anang and J. I. Han, Facilely Synthesized NiMoO4/CoMoO4 Nanorods as Electrode Material for High Performance Supercapacitor, *J. Alloys Compd.*, 2018, **742**, 342–350.

36 Y. Ren, J. Wang, W. Hu, H. Wen, Y. Qiu, P. Tang, M. Chen and P. Wang, Hierarchical Nanostructured Co-Mo-B/CoMoO4-x Amorphous Composite for the Alkaline Hydrogen Evolution Reaction, *ACS Appl. Mater. Interfaces*, 2021, **13**(36), 42605–42612.